Posted: March 1, 2021

A strain-based investigation of the accuracy of embedded markers used in tracking cadaveric brain motion

Scott Dutrisac[1], T. Blaine Hoshizaki[2], and Oren E. Petel[1,*]

[1]Department of Mechanical and Aerospace Engineering, Carleton University, Ottawa, ON, Canada K1S 5B6
[2]School of Human Kinetics, University of Ottawa, Ottawa, ON, Canada K1S 5S9
[*]Corresponding author: oren.petel@carleton.ca

Abstract

Measurements of intracranial brain displacement in cadaveric specimens have been instrumental to the validation finite element (FE) models of brain injury. These data collections have used radiographic and sonomicrometric techniques, requiring the use of tissue-embedded tracking markers; however, marker accuracy has never been adequately characterized. Marker tracking precision has been erroneously conflated with measurement accuracy, not accounting for changes in the natural response of surrounding tissues due to marker presence. Non-negligible inertia, high stiffness, and the aspect ratio of markers all contribute to this interference. This work investigated the dynamic coupling between published marker designs (NDTs, Sonomicrometry Crystals, and Tin) and a new elastomeric marker, and a block of tissue simulant subjected to a drop impact. The measured strains were compared to the baseline response of the simulant containing massless markers. The results found notable evidence of interference in simulant strain amplitudes as well as considerable directional bias in the response of some markers. The elastomeric marker was found to have minimal interference in the deformation field. Future FE model validation will need to account for the considerable interference and directional biases to the natural response of brain tissue in existing cadaveric datasets to maintain confidence in strain predictions.

1 Introduction

The bulk kinematic mechanisms behind brain trauma have been developed through investigations observing brain motion in animal models. From these earliest animal models, it was shown that an impulsive acceleration of the head results in a differential bulk motion of the brain within the skull (Pudenz and Shelden, 1946; Shelden et al., 1944) and that rotational acceleration of the head was highly correlated to diffuse brain injury (Holbourn, 1943; Ommaya and Gennarelli, 1974). Further insights into the dynamic response of the brain to impulsive acceleration have been gained through intracranial measurements of brain tissue displacement and deformation in Post-Mortem Human Surrogates (PMHS). These intracranial measurements have been made using high-speed radiographic (Al-Bsharat et al., 1999; Guettler, 2017; Hardy et al., 2001, 2007) and sonomicrometry techniques (Alshareef et al., 2018, 2020). Each of these techniques require the installation of embedded markers or targets within the brain tissue that were used to track tissue response in areas that are visually inaccessible using traditional optical methods. These data were used extensively in the validation of finite element (FE) head injury models (Ji et al., 2015; Kleiven and Hardy, 2002; Takhounts et al., 2008; Zhao and Ji, 2020; Zhou et al., 2019); however, the accuracy of these methods as a result of the marker design choices has never been adequately characterized. Error quantification relating to the interference of these markers in the natural response of brain tissues to mechanical perturbation is critical to the validity of FE models and their injury predictions, as well as our broader understanding of brain trauma and injury. In the present study, we investigated the dynamic coupling between a variety of embedded marker designs used in prior PMHS brain displacement studies against the response of massless markers in a drop-impacted tissue-simulating gel to quantify marker interference in the resulting deformation field.

The calibration and validation of FE models (Ghajari et al., 2017; Giordano and Kleiven, 2014; Giudice et al., 2019; Ji et al., 2014, 2015; Patton et al., 2013; Post and Hoshizaki, 2015; Post et al., 2019; Takhounts et al., 2008; Zhao et al., 2017; Zhao and Ji, 2020; Zhou et al., 2019) have relied heavily on the PMHS datasets

available in the literature (Alshareef et al., 2018, 2020; Hardy et al., 2001, 2007; Nahum et al., 1977). Despite relying on the same datasets for calibration, a comparison of two computational head injury models, resulted in peak Maximum Principal Strain (MPS) values that differed by anywhere from 50 to 100% in their intracranial strain predictions, for the same input head kinematics (Beckwith et al., 2018). These authors suggested that these variations in FE model intracranial strain predictions were the result of differences in brain geometry and model boundary conditions. Zhao and Ji (Zhao and Ji, 2020) noted that current FE model validation efforts rely on comparisons to brain tissue strain measurements with insufficient spatial resolution for an effective validation under a variety of medium- and high-strain rate loading conditions. While spatial resolution is a limitation that must be overcome in future datasets, the difference in strain predictions based on existing datasets may be evidence of a deeper limitation related to the accuracy of existing measurements of brain tissue motion and deformation.

The precision of marker tracking methods have been quantified in prior work (Alshareef et al., 2018); however, the quoted precision of these techniques were not a true measure of the accuracy of these measurements in brain tissue under dynamic loading, as these estimates are based on static marker localization precision. Markers embedded in tissues have their own inertia, and as a result, their presence will necessarily change the response of brain tissue to impulsive mechanical perturbation. As such, much of the literature has conflated tracking precision with the accuracy of tissue deformation measurements, and a lack of marker migration within tissue as proof of the fidelity of dynamic marker coupling. While Whyte et al. (Whyte et al., 2019) have shown that some markers do migrate within brain tissue, which is undesirable, this is not the only measure of accuracy relating to the dynamic coupling of an embedded marker within tissues. The mere presence of markers, having their own inertia and stiffness, will change the displacement and deformation fields of the surrounding tissues, and the true measure of the accuracy of the method is related to minimization and quantification of this interference (Dutrisac et al., nd). It is not sufficient to precisely know the position of a marker, if that marker is in the wrong position due to its interference in the natural deformation field. A recent study investigated the optimization of embedded markers within a tissue simulant, finding that a range of marker parameters (density, stiffness, and spacing) significantly altered the displacement field in the surrounding matrix (Dutrisac et al., nd). The authors of that study suggested optimal density and stiffness ranges for such markers, which were the basis for a new radiopaque marker design used in the present work.

In the present study, we investigated the accuracy of embedded markers, designs that have been used to track tissue deformation in prior PMHS studies, in measuring a dynamic 2-D strain field within a block of tissue simulant. The markers, some of which had an elongated aspect ratio, were tested in different orientations to determine whether they produced an anisotropic, directionally biased, interference in the natural deformation field of the tissue simulant. Comparisons were made to the deformation of a block of tissue simulant having a series of massless markers, which was taken as a baseline natural response of the matrix, as well as a proposed radiopaque marker designed for future PMHS studies. The primary objectives of this work were to determine the accuracy and directionality of the response of markers used to track PMHS brain response in prior studies, which may explain some of the disparity in strain responses predicted by FE models. This data, investigating the response variability of these markers, will be essential to the future calibration and validation of FE models of head injury used in protective equipment design and brain injury prevention efforts.

2 Materials and Methods

Three embedded marker types that have been used in prior PMHS investigations were considered in the present comparison. These three markers were the Neutral Density Targets (NDTs) used by Hardy et al. (Hardy et al., 2001, 2007), the Sonomicrometry Crystals (SMC) used by Al-Shareef et al. (Alshareef et al., 2018, 2020), and the tin granules used by Guettler (Guettler, 2017). In addition to those established marker designs, we will investigate a novel elastomeric marker that was designed specifically for PMHS brain tissue studies, which will be referred to as the Carleton Elastomeric Marker (CEM) (Dutrisac et al., nd). This elastomeric marker was optimized using the results of a parametric study on embedded marker properties (Dutrisac et al., nd). Once prepared, each marker type was cast into the central plane of a block of tissue-simulant, Humimic #4. This tissue-simulant had a density of 0.85 g/cm^3 and an elastic modulus of approximately 9 kPa, based on the manufacturer supplied durometer of 11.8 (Shore OO) (Larson, 2017; Mix and Giacomin, 2011), which is the same order of magnitude as the elastic modulus of brain tissue (Budday et al., 2015). Schematics of the block and marker designs are shown in Fig. 1 and Fig. 2, respectively.

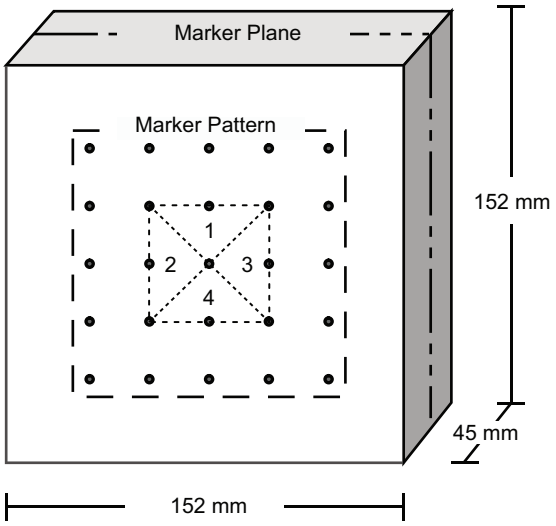

Figure 1: A schematic of the tissue simulant block, marker arrangement, and elements used in the strain calculation.

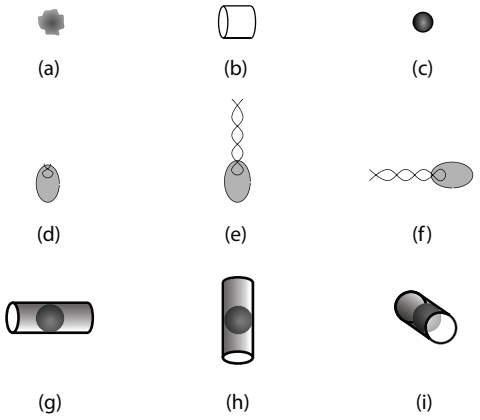

Figure 2: A schematic of the markers used in the present work: (a) Massless marker; (b) Carleton Elastomeric Marker; (c) Tin Marker; (d) SMC - no wire; (e) SMC - vertical wire; (f) SMC - horizontal wire; (g) NDT - horizontal orientation; (h) NDT - vertical orientation; (i) NDT - transverse orientation. Note that all markers were drawn to scale.

Table 1: Summary of marker mechanical and geometric properties

Marker	Density (g/cm^3)	Elastic Modulus (MPa)	Geometry	Aspect Ratio
Massless	-	-	-	-
NDT	1.5	200	Cylinder	2.5
SMC	1.1	10	Bulb and wire	1
Tin	7.3	41,600	Sphere	1
CEM	1.6	0.012	Cylinder	1

2.1 Marker and block preparation

Each set of embedded markers was prepared according to descriptions found in the literature, with an effort to maintain their size, density, and stiffness characteristics based on the available materials. The NDT markers were each composed of a thin-walled polyethylene tube 5 mm in length with a 1.5 mm diameter. The low-density polyethylene is less stiff than the polystyrene (E =3.5 GPa) described by Hardy et al. (Hardy et al., 2007), however it is still several orders of magnitude stiffer than the matrix material. A 1.5 mm long, 1.5 mm diameter piece of 97%-Sn-3%-Cu solder wire was cut and inserted into each tube. Tubes were sealed using cyanoacrylate adhesive. The SMC markers were replicated using an amine epoxy (3M DP 420, Dow Inc.) and a twisted pair signal cable (34 AWG, PTFE Jacket, Daburn Electronics). These components are identical to those used in the off-the-shelf sonomicrometry crystals used by Al-Shareef et al. (Alshareef et al., 2018, 2020). Pre-cut 300 mm lengths of twisted pair cable were dipped in uncured epoxy, building up a bulbous capsule at the tip. This process was repeated until bulbs of approximately 1.5 to 2 mm diameter were achieved and dipped wires were left to fully cure. The SMCs without a signal wire were created in the same fashion, however the excess wire was cut once the capsule was fully cured. The tin granules used by Guettler (Guettler, 2017) were formed from a 97$\%$-Sn-3$\%$-Cu solder wire. Pre-cut 3 mm lengths of solder wire cut and heated using a fine point soldering tip until liquefied. Once liquefied, the surface tension of the molten material pulled it into a spherical granular form which was left to cool. While these granules were not pure tin, given the relatively small amount of alloying material, the density remained consistent with pure tin (7.3 g/mL). Carleton Elastomeric markers were a blend of thermoplastic gel (Humimic $\#$4) and a powdered contrast agent ($BaSO_4$). A mixture of 60 wt$\%$ $BaSO_4$ was used for the present investigation. Gel material was melted at 160°C and mixed with $BaSO_4$ powder. The mixture was pressed into a precision machined brass mould. The mould was left to set at room temperature for 24 hours. Once set, a sheet of 2 mm-diameter and 2 mm-long cylindrical markers was removed from the mould. Massless markers were made from alcohol-based ink (Sharpie) drawn approximately 2 mm in diameter. A summary of marker properties can be found in Table 2.1. It should be noted that while the wire-free SMCs had an aspect ratio of 1, the wired version could be considered as a non-unity aspect ratio.

Insertion of markers into tissue-simulant blocks would damage the surrounding material and obscure the required optical clarity. Instead, markers were prepared in advance and cast into the simulant blocks. A mould constructed from a 1:1 blend of Sylgard 184 and 527 was used to produce the tissue simulant blocks; this material provided necessary heat resistance for the melted material while remaining flexible for demoulding. Blocks measured 152 mm $\times$ 152 mm $\times$ 45 mm (Fig. 1). Thermoplastic tissue-simulant gel (Humimic $\#$4) was slowly melted in a ceramic crucible and agitated to remove large air bubbles. Once fully liquefied, the gel was poured into the mould, filling it half way, agitated again to remove entrapped air and was left to set. The surface of the half filled mould was used as the marker plane. A template was placed on top of the surface and registration marks were drawn to ensure even placement of markers. Markers were placed in a 5$\times$5 grid, with 20 mm spacing. The surface was lightly heated to allow local melting, allowing placed markers to stay in place during the pattern assembly. Once all markers were placed, additional melted tissue simulant gel was poured into the mould, filling it completely. The mould was agitated again to remove larger air bubbles, and the remaining air bubbles were removed manually. The wires attached to SMC markers were coated with a release agent (Ease Release 200) to prevent the tissue simulant from bonding to them, as bonding between the wire and surrounding matrix would not have been consistent with their use in PMHS testing. SMC and NDT markers were tested in various orientations due to their non-unity aspect ratios. For each of these markers, vertical and horizontal orientations were achieved by rotating the same test block 90° within the drop-housing. The wire-free SMC markers were cast separately from the wired version. Similarly, for the NDTs in the transverse orientation, a separate tissue simulant block was produced.

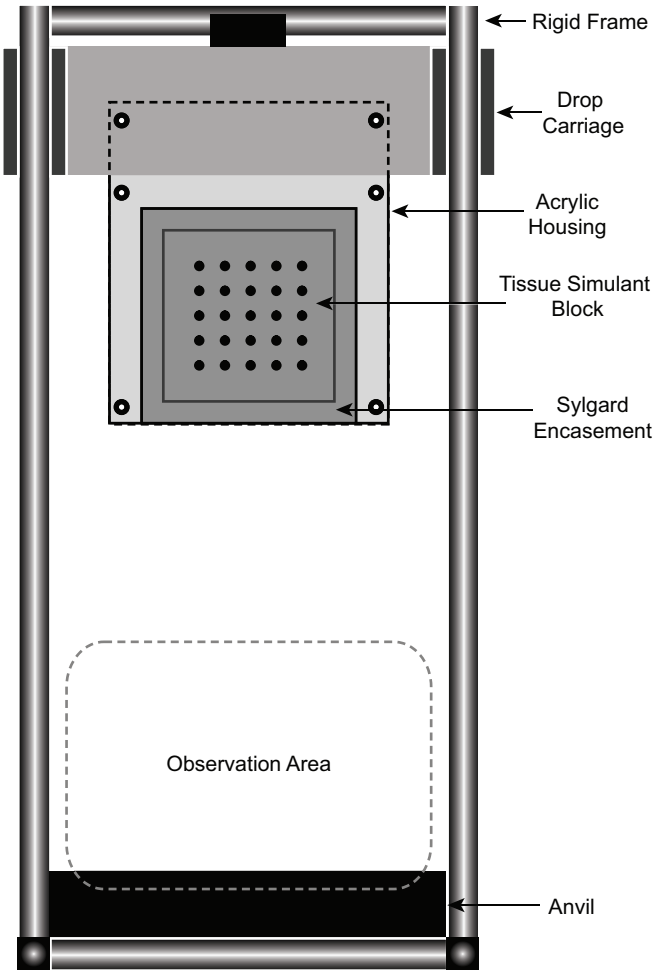

Figure 3: A schematic of the drop assembly used in the investigation.

2.2 Drop testing and data capture

The impact response of the tissue simulant blocks was tested by subjecting each to a series of 3 independent vertical drops from a height of 84.0 $\pm$ 0.3 cm onto a rigid anvil using a custom drop-tower (Fig. 3). To protect against boundary damage, blocks were placed within the Sylgard mould used in the casting process. The block and mould assembly was sandwiched between plates of acrylic. These plates restricted out of plane motion and buckling of the specimen blocks. The total thickness of the blocks and acrylic plates was maintained precisely at 47 mm to ensure a reproducible clamping strength and the consistency of the boundary conditions. Each specimen assembly was assessed for damage and slippage within the housing between repeated drop tests.

The impact and deformation of the tissue simulant blocks were captured using a high-speed video camera (NAC HX-3) at a frame rate of 7,500 fps for a period of 200 ms with a 25$\%$ pretrigger. To achieve sufficient image contrast, a white, translucent paper membrane was applied to the specimen housing and back-lit using a 2000 lumen LED lighting fixture (Cinema Work Light, MossLED Inc.).

2.3 Analysis

The videos of the impact events were processed for to measure marker displacement and calculate strain using a custom particle tracking code that has been validated in prior work (Dutrisac, 2020). A set of non-deforming fiducial markers on the drop carriage assembly was tracked, enabling us to precisely determine the moment of impact as well as to subtract rigid body motion from the analysis. Standardizing the deformation across the sample set, these fiducial markers were also used to develop a relative pixel-to-millimetre scale for each specimen. For the Massless, CEM, and SMC specimens, the scale was 4.25 $\pm$ 0.01 px/mm, while for NDT and tin specimens, the scale was 4.69 $\pm$ 0.01 px/mm.

For consistency, the comparisons were made through an analysis of the motion of the central markers to avoid lateral boundary influences. The pre-impact position of these markers was used as a baseline to determine post-impact displacement with the block. The positions of the nine central markers, forming a 3×3 grid, were tracked through the video frames using the particle tracking code. The displacements of these markers were used to calculate the elemental strain in the central region based on a definition of 4 triangular elements, as illustrated in Fig. 1. The method is similar to that proposed in previous work related to brain-tissue strain (Zhou et al., 2019). The strain was determined using a 2D polynomial fit to the triangular element described by the nodal markers (Pan, 2007),

$$u[x,y] = a_0 + a_1 x + a_2 y, \tag{1}$$

$$v[x,y] = b_0 + b_1 x + b_2 y, \tag{2}$$

where u and v are the displacement vectors of each node at position (x,y) and (a_0,a_1,a_2,b_0,b_1,b_2) are coefficients used in the strain tensor. Once fitted, the polynomial coefficients are solved using marker displacement data and Green-Lagrangian strain is calculated using the expressions,

$$\begin{aligned} \epsilon_{xx} &= \frac{\partial u}{\partial x} + \frac{1}{2}\left[\left(\frac{\partial u}{\partial x}\right)^2 + \left(\frac{\partial v}{\partial x}\right)^2\right], \\ \epsilon_{yy} &= \frac{\partial v}{\partial y} + \frac{1}{2}\left[\left(\frac{\partial u}{\partial y}\right)^2 + \left(\frac{\partial v}{\partial y}\right)^2\right], \\ \epsilon_{xy} &= \frac{1}{2}\left(\frac{\partial u}{\partial y} + \frac{\partial v}{\partial x}\right) + \frac{1}{2}\left[\frac{\partial u}{\partial x}\frac{\partial u}{\partial y} + \frac{\partial v}{\partial x}\frac{\partial v}{\partial y}\right], \end{aligned} \tag{3}$$

where ϵ_{xx}, ϵ_{yy}, and ϵ_{xy} are the respective directional and shear strains. The Maximum Principal Strain (MPS) can then be determined from the equation,

$$\epsilon_{MPS} = \frac{\epsilon_{xx} + \epsilon_{yy}}{2} + \sqrt{\left(\frac{\epsilon_{xx} - \epsilon_{yy}}{2}\right)^2 + \left(\frac{\epsilon_{xy}}{2}\right)^2}, \tag{4}$$

where ϵ_{MPS} represents the maximum principal strain. The averaged MPS response across the 4 triangular elements were then used to determine the strain response at the centre of the tissue simulant block. The averaged MPS response was determined and reported for each drop event and was used to draw comparisons of marker influence on the tissue simulant deformation across the samples.

3 Results

The strain response data are shown separately for each embedded marker type and orientation. The baseline response of the tissue simulant from each drop, which was tracked using massless markers, is shown in Fig. 4. Each solid curve in this figure represents the average strain values determined from a single drop test, while the dashed curve represents the average response of all drop tests recorded. The massless marker system exhibited multiple identifiable strain maxima and minima in the first 40 ms following impact, the timing and shape of which were consistent across the three tests conducted. The variability of the strain measurement within the first two peaks were particularly minimal, but diverged to a greater extent after 25 ms. These results demonstrate the high level of reproducibility between the drop tests. The average response curve in Fig. 4 will be used as a comparison basis against the other embedded markers tested to determine their interference in the natural deformation response of the tissue simulant. Deviations from this average massless marker response will be interpreted as evidence of embedded marker interference.

The strain responses measured with the NDTs (Hardy et al., 2001, 2007) are shown separately for NDTs mounted in a horizontal (Fig. 5a), vertical (Fig. 5b), and transverse (Fig. 5c) orientation and were compared to the baseline response of the tissue simulant matrix. The strain response of the matrix with embedded NDTs had the same general shape as its baseline response, although the amplitudes of the peak strains varied appreciably, particularly in the vertical and transverse orientations. The NDTs consistently damped the initial strain peak in the matrix, underestimating it, and then rebounded in a manner that extended the tensile strain in the matrix at the second peak. Subsequent peaks were inconsistent with the matrix response both temporally and in terms of strain magnitudes. The overall interference of the NDTs in the natural response of the tissue simulant matrix was strongly directionally dependent.

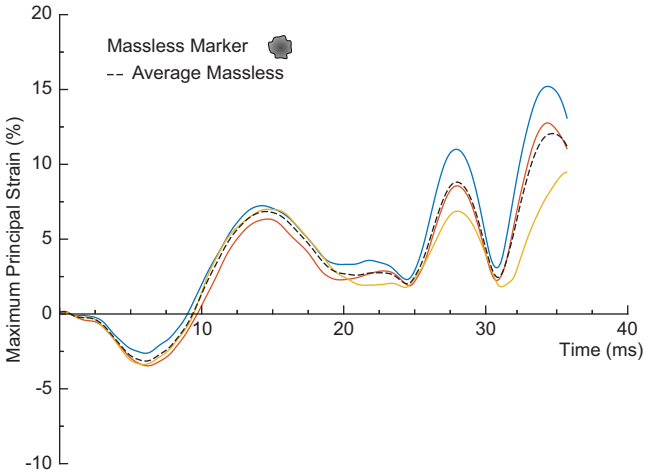

Figure 4: The maximum principal strain response measured from the baseline massless markers for three separate drop impacts. An averaged response of the massless markers is shown as a dashed line.

The SMCs (Alshareef et al., 2018, 2020) were investigated in several configurations, one of which did not include wiring and two that included wiring in two different orientations. In PMHS experiments, these crystals were wired to a diagnostic setup (Alshareef et al., 2018, 2020), so the influence of the wiring on the tissue simulant matrix deformation is of considerable importance. The performance of the SMCs themselves, without wiring or barbs, are provided in Fig. 6a. The strain response with these crystals was similar to that of the NDTs, where the first strain peak was notably damped by the presence of the crystals, but then the subsequent strain peak had extended the tensile strain in the matrix. With the addition of the wiring, the response became considerably anisotropic, having a directionally dependent response. With the wire oriented in the vertical direction (Fig. 6b), the same damped response of the first peak and extension of the second peak was observed as it had been for the crystal without a wire (Fig 6a). One major change in the response of the matrix deformation with a crystal having a vertically-oriented wire was seen beyond 20 ms, where the presence of the wire damped the further motion of the matrix. For the SMC, having wires oriented in the horizontal direction (Fig. 6c), the response of the matrix was completely altered, changing the frequency of the strain response and damping many of the strain peaks.

The strain responses measured with tin markers (Guettler, 2017) are shown in Fig. 7. These tin markers resulted in a deformation response of the tissue-simulant matrix with the highest degree of magnitude variability. The same general trends of a damped first strain peak and over-extended tensile deformation at the second peak.

The final marker that was tested was the Carleton Elastomeric Marker (Dutrisac, 2020), the results for which are shown in Fig. 8. The tissue simulant matrix response with this embedded marker was extremely similar to the natural response of the matrix, exhibiting a similar level of scatter around the baseline average strain values. The measured strain response in the tissue simulant matched the shapes and magnitudes of the peak strain values of the neat materials for the entire observation window. The only clear difference in the response of the matrix using this embedded marker was a time shift of the tertiary strain peaks that appeared 22 ms following the impact. This marker resulted in the lowest variability in its measured strain response among the markers investigated.

4 Discussion

As a first order comparison of the interference of the various embedded markers in the deformation of the tissue simulant, the first and second peaks strain values (occurring at approximately 5 ms and 15 ms, respectively) are shown in a series of bar charts Fig. 9a and Fig. 9b, respectively. This comparison illustrates the variability of the deformation measured in comparison to the neat matrix, as well as the directionality of this interference. None of the markers used in prior PMHS studies lay consistently within the strain bounds of the response of the neat matrix tracked using massless markers. The only marker that provided a similar response, with identical bounds of performance were the Carleton Embedded Markers, which were designed based on the guidance a parametric study of optimal material properties (Dutrisac et al.,

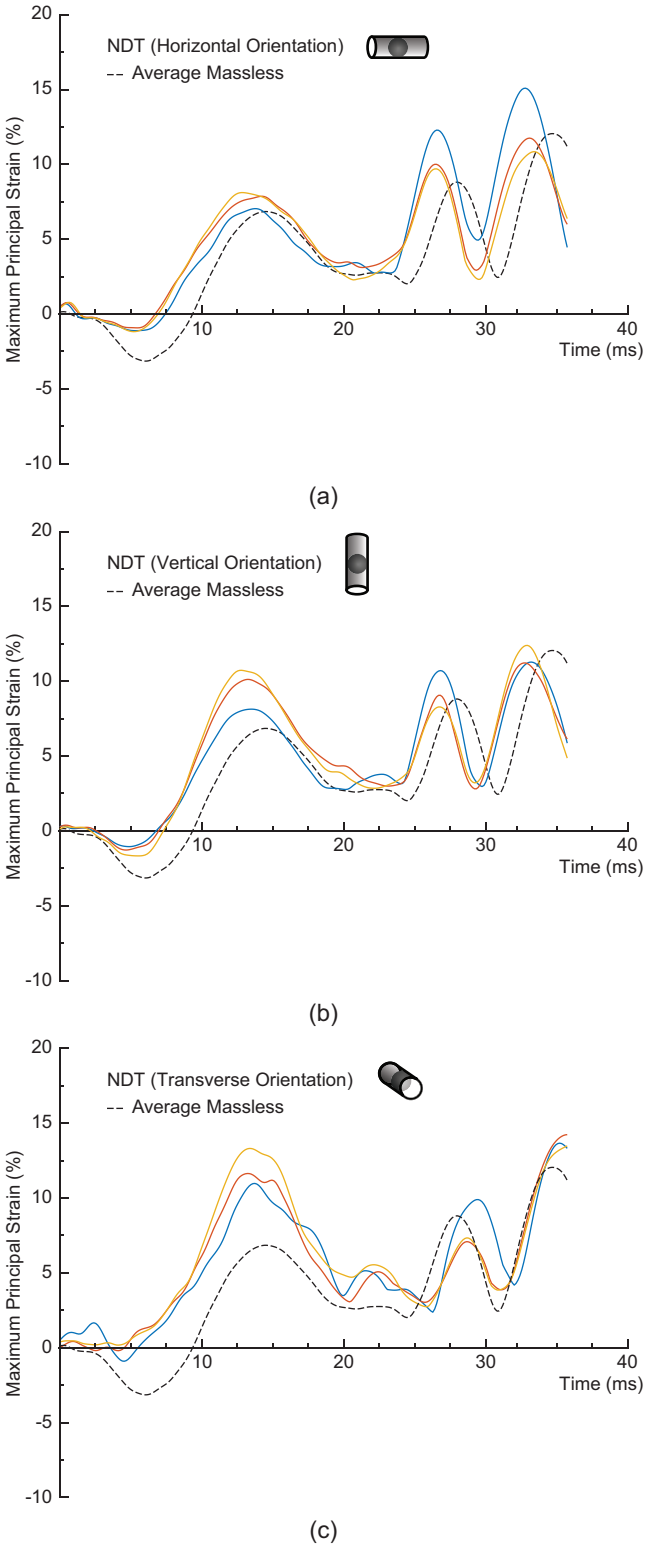

Figure 5: The maximum principal strain response measured from the motion of the NDT markers used by Hardy et al. (Hardy et al., 2001, 2007) for three separate drop impacts in (a) a horizontal orientation; (b) a vertical orientation; and (c) a transverse orientation. The averaged response of the massless markers from Fig. 4 is included as a dashed line for comparison.

nd).

The parametric study of optimal material properties found that the ideal range of marker stiffness involved an elastic modulus of less than 1 MPa and a suggested marker-to-tissue density ratio of below

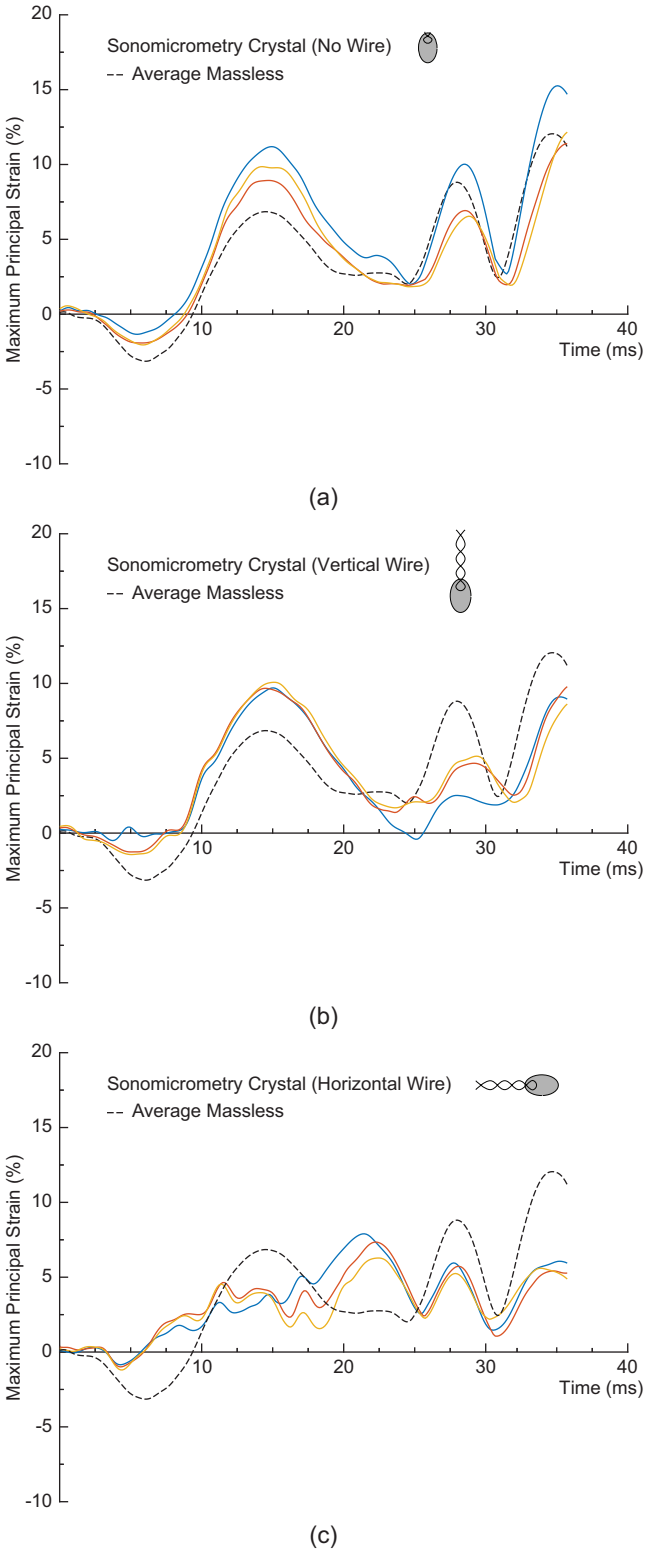

Figure 6: The maximum principal strain response measured from the motion of the sonomicrometry crystals used by Al-Shareef et al. (Alshareef et al., 2018, 2020) for three separate drop impacts with (a) crystals having no wire; (b) crystals having vertical wires; and (c) crystals having horizontal wires. The averaged response of the massless markers from Fig. 4 is included as a dashed line for comparison.

1.7 (Dutrisac et al., nd). Embedded markers outside of these ranges were found to deviate considerably from the response of non-inertial markers. Those findings were consistent with the observations made in this dataset.

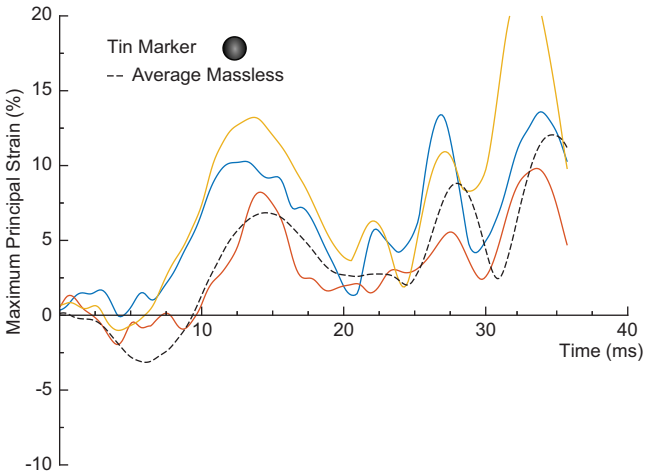

Figure 7: The maximum principal strain response measured from the motion of the tin granule markers used by Guettler (Guettler, 2017) for three separate drop impacts. The averaged response of the massless markers from Fig. 4 is included as a dashed line for comparison.

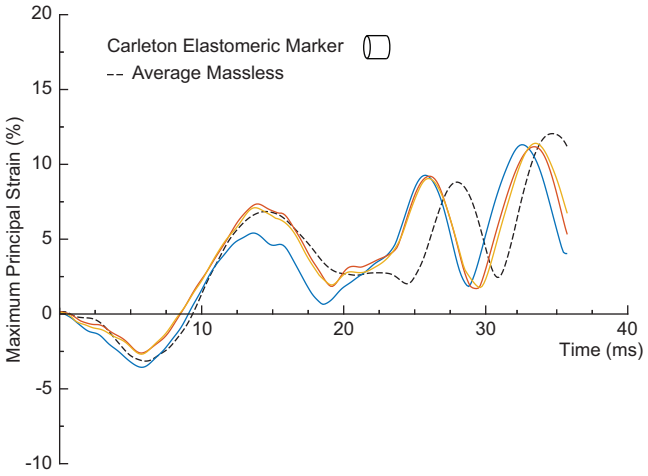

Figure 8: The maximum principal strain response measured from the motion of the Carleton Elastomeric Markers designed based on the marker design sensitivity study by Dutrisac et al. (Dutrisac et al., nd) for three separate drop impacts. The averaged response of the massless markers from Fig. 4 is included as a dashed line for comparison.

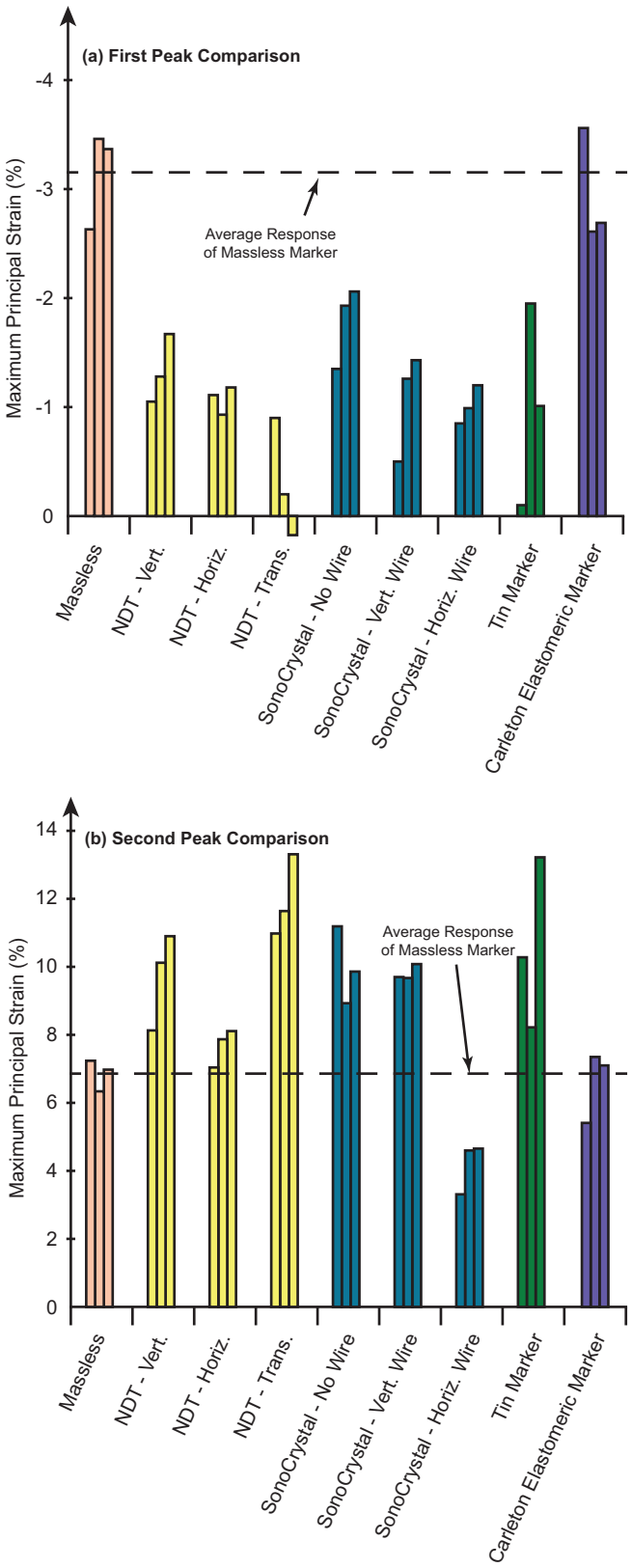

Figure 9: A bar chart comparison of the measured strains using the various embedded markers for the (a) first strain peak and (b) second strain peak. The dashed line represents the average value taken from the massless marker data shown in Fig 4.

The NDTs had a density of 1.5 g/cm^3, an elastic modulus of approximately 200 MPa (based on the polyethylene exterior), and an length-to-diameter aspect ratio of 2.5 (Hardy et al., 2001, 2007). While the NDTs were within the optimal density range, the high stiffness of these markers resulted in significant interference in the deformation pattern of the tissue simulant (Fig. 5). Furthermore, the variability of the strain response in the three orientations tested was due to a combination of their aspect ratio and the anisotropy in the stiffness of the NDTs along the different axes. The block used in the horizontal and vertical orientations was the same block of simulant rotated 90 degrees, so these differences were not related to manufacturing variability. As a result, the strain response measured using this marker was highly dependent on its orientation, a variability that must be considered in the analysis and implementation of this dataset into future FE model validation.

The SMCs (Alshareef et al., 2018, 2020) had a density of 1.13 g/cm^3, an elastic modulus of approximately 10 MPa, an aspect ratio of unity, and the addition of wiring. While the density of these markers was also within the recommended range, their stiffness was higher than the recommended marker stiffness bound (Dutrisac et al., nd). This high stiffness explains the interference of these markers in the deformation of the tissue simulant seen in Fig. 6a, which was similar to the interference of the NDTs. While the aspect ratio of the markers themselves was 1 for this investigation, these crystals have previously been used in a barbed configuration (Alshareef et al., 2018, 2020) which may result in a directionally-dependent interference in tissue deformation, although this has not been quantified in the present work. That being said, the present work did investigate the influence of the wires attaching to these crystals, which are required for their operation (Alshareef et al., 2018, 2020). The wires were able to slide easily within paths made for them, but despite this ease of motion, the presence of horizontal wires completely changed the deformation pattern in the tissue simulant (Figs. 6a and 6b). Once again, the same test assembly was used in both orientations to ensure that the results were not due to any variability in sample construction, yet the directional influence of the wires on the deformation of the brain simulant was pronounced.

The tin markers had a density of 7.3 g/cm^3, an elastic modulus of approximately 41.6 GPa, and an aspect ratio of unity (Guettler, 2017). While they were extremely small to reduce their inertia, this did not prevent their influence on the dynamic deformation of the tissue simulant (Fig. 7). This influence appeared to be the result of a competition between the damping response of their high density and the influence of their stiffness on the deformation of the tissue simulant, which was consistent with prior observations (Dutrisac et al., nd). The competition between the role of density and stiffness in interfering with the deformation of the tissue simulant was likely a factor in the higher strain variability in this dataset, compared to that of other markers.

The Carleton Elastomeric Markers had a density of 1.6 g/cm^3, an elastic modulus of approximately 12 kPa, and an aspect ratio of unity. These markers are at the edge of the acceptable density range, but within the recommended stiffness range (Dutrisac et al., nd). The interference between these markers and the matrix tissue simulant was minimal (Fig. 8). These markers offered the best performance of the marker designs investigated with strain field bounds that perfectly matched those of the baseline test system and were designed for future use in PMHS experiments.

These results reinforce the concept that the accuracy of dynamic deformation measurements is not only guided by the precision of a measurement, but the interference of the technique on the measurement. The introduction of an inertially significant target within a material will affect the deformation of the matrix it is embedded within. Ensuring lack of marker migration is only one consideration in the dynamic coupling of a material. Under quasi-static conditions, proper coupling of a gauge to a material will ensure that the two materials experience the same strains. In dynamic conditions, a large disparity in the marker and matrix stiffnesses will result in an associated strain disparity that will change the dynamic response of the matrix. Future PMHS studies observing dynamic tissue deformation should focus on the use of freely suspended, neutral density, and neutral stiffness markers (e.g., Carleton Elastomeric Marker) with an aspect ratio of unity to ensure uniform and minimal interference tracking of tissue deformation.

Given the similarity of the material properties of brain tissue and the tissue simulant used in this research, we expect that these results would accurately inform the marker response within PMHS brain tissue. From an FE model validation perspective, the results demonstrate that the existing PMHS datasets have inherent directionally-dependent biases that must be accounted for in future validation work. The embedded markers that have thus far been used in PMHS brain motion studies were likely to have interfered with the dynamic tissue response of the PMHS brains. This interference resulted in measurement inaccuracies and uncertainties that have yet to be considered or fully quantified, but are more significant than the tracking precision of any individual method. Due to the anisotropic interaction between the markers and the tis-

sues, care must be taken to properly account for these biases inherent in the existing three-dimensional datasets to recover an adequate representation of the natural deformation response of brain tissues. While the differences in strain predictions made with various FE models are notable (Beckwith et al., 2018), perhaps these differences may be at least partially explained by these issues of accuracy and directional bias of the interference of embedded markers on the tissue deformation captured in the existing datasets (Fig. 9). Properly accounting for the true anisotropic accuracies of existing PMHS data will be necessary to maintain confidence in the validation of FE model strain predictions.

5 Acknowledgments

The authors thank Sheng Xu and Jennifer Rovt for their insights and useful feedback on the experiment and its interpretation, and MacKenzie Brannen for assistance with specimen preparation. This work was funded by the CIHR and NSERC through the Collaborative Health Research Program (CPG-151967). The high-speed camera was purchased with funds from the Canada Foundation for Innovation and Ontario Research Fund (Project 32933). SD received funding through the Ontario Graduate Scholarship.

References

Al-Bsharat, A. S., Hardy, W. N., Yang, K. H., Khalil, T. B., Tashman, S., and King, A. I. (1999). Brain/skull relative displacement magnitude due to blunt head impact: New experimental data and model. *Stapp Car Crash Conference Proceedings*, P-350(724):321–332.

Alshareef, A., Giudice, J. S., Forman, J., Salzar, R. S., and Panzer, M. B. (2018). A novel method for quantifying human in situ whole brain deformation under rotational loading using sonomicrometry. *Journal of Neurotrauma*, 35(5):780–789.

Alshareef, A., Giudice, J. S., Forman, J., Shedd, D. F., Reynier, K. A., Wu, T., Sochor, S., Sochor, M. R., Salzar, R. S., and Panzer, M. B. (2020). Biomechanics of the human brain during dynamic rotation of the head. *Journal of Neurotrauma*, 37(13):1546–1555.

Beckwith, J. G., Zhao, W., Ji, S., Ajamil, A. G., Bolander, R. P., Chu, J. J., McAllister, T. W., Crisco, J. J., Duma, S. M., Rowson, S., Broglio, S. P., Guskiewicz, K. M., Mihalik, J. P., Anderson, S., Schnebel, B., Brolinson, P., Collins, M. W., and Greenwald, R. M. (2018). Estimated brain tissue response following impacts associated with and without diagnosed concussion. *Annals of Biomedical Engineering*, 46(6):819–830.

Budday, S., Nay, R., de Rooij, R., Steinmann, P., Wyrobek, T., Ovaert, T. C., and Kuhl, E. (2015). Mechanical properties of gray and white matter brain tissue by indentation. *Journal of the mechanical behavior of biomedical materials*, 46:318–330.

Dutrisac, S. (2020). *A Study of the Impact Response of Discrete Regions of the Human Cadaver Brain*. Master's Thesis, Carleton University.

Dutrisac, S., Brannen, M., Hoshizaki, T. B., Frei, H., and Petel, O. E. (nd). A parametric analysis of embedded tissue marker properties and their effect on the accuracy of displacement measurements. *engrXiv. engrxiv.org/ksq7p*.

Ghajari, M., Hellyer, P. J., and Sharp, D. J. (2017). Computational modelling of traumatic brain injury predicts the location of chronic traumatic encephalopathy pathology. *Brain*, 140:333–343.

Giordano, C. and Kleiven, S. (2014). Evaluation of axonal strain as a predictor for mild traumatic brain injuries using finite element modeling. *Stapp Car Crash Journal*, 58:29–61.

Giudice, J. S., Zeng, W., Wu, T., Alshareef, A., Shedd, D. F., and Panzer, M. B. (2019). An analytical review of the numerical methods used for finite element modeling of traumatic brain injury. *Annals of Biomedical Engineering*, 47(9):1855–1872.

Guettler, A. J. (2017). *Quantifying the Response of Relative Brain/Skull Motion to Rotational Input in the PMHS Head*. Master's Thesis, Virginia Polytechnic Institute and State University.

Hardy, W. N., Foster, C. D., Mason, M. J., Yang, K. H., King, A. I., and Tashman, S. (2001). Investigation of head injury mechanisms using neutral density technology and high-speed biplanar x-ray. *Stapp Car Crash Journal*, 45:337–368.

Hardy, W. N., Mason, M. J., Foster, C. D., Shah, C. S., Kopacz, J. M., Yang, K. H., King, A. I., Bishop, J., Bey, M., Anderst, W., and Tashman, S. (2007). A study of the response of the human cadaver head to impact. *Stapp Car Crash Journal*, 51:17–80.

Holbourn, A. H. S. (1943). Mechanics of head injuries. *The Lancet*, 242(2627):438–441.

Ji, S., Ghadyani, H., Bolander, R. P., Beckwith, J. G., Ford, J. C., McAllister, T. W., Flashman, L. A., Paulsen, K. D., Ernstrom, K., Jain, S., and Raman, R. (2014). Parametric comparisons of intracranial mechanical responses from three validated finite element models of the human head. *Annals Biomedical Engineering*, 42(1):11–24.

Ji, S., Zhao, W., Ford, J. C., Beckwith, J. G., Bolander, R. P., Greenwald, R. M., Flashman, L. A., Paulsen, K. D., and McAllister, T. (2015). Group-wise evaluation and comparison of white matter fiber strain and maximum principal strain in sports-related concussion. *Journal of Neurotrauma*, 32(7):441–454.

Kleiven, S. and Hardy, W. N. (2002). Correlation of an fe model of the human head with local brain motion: Consequences for injury prediction. *Stapp Car Crash Journal*, 46:123–144.

Larson, K. (2017). *Can you estimate modulus from durometer hardness for silicones?* Dow Chemical Company, Technical Report.

Mix, A. W. and Giacomin, A. J. (2011). Standardized polymer durometry. *Journal of Testing and Evaluation*, 39(4):1–10.

Nahum, A. M., Smith, R., and Ward, C. C. (1977). Intracranial pressure dynamics during head impact. *SAE Technical Paper*, page 770922.

Ommaya, A. K. and Gennarelli, T. A. (1974). Cerebral concussion and traumatic unconsciousness: correlation of experimental and clinical observations of blunt head injuries. *Brain*, 97:633–654.

Pan, B. (2007). Full-field strain measurement using a two-dimensional savitzky-golay digital differentiator in digital image correlation. *Optical Engineering*, 46(3):033601.

Patton, D. A., McIntosh, A. S., and Kleiven, S. (2013). The biomechanical determinants of concussion: Finite element simulations to investigate brain tissue deformations during sporting impacts to the unprotected head. *Journal of Applied Biomechanics*, 29(6):721–730.

Post, A. and Hoshizaki, T. B. (2015). Rotational acceleration, brain tissue strain, and the relationship to concussion. *Journal of Biomechanical Engineering*, 137(3):030801.

Post, A., Hoshizaki, T. B., Karton, C., Clark, J. M., Dawson, L., Cournoyer, J., Taylor, K., Oeur, R. A., Gilchrist, M. D., and Cusimano, M. D. (2019). The biomechanics of concussion for ice hockey head impact events. *Computer Methods in Biomechanics and Biomedical Engineering*, 22(6):631–643.

Pudenz, R. H. and Shelden, C. H. (1946). The lucite calvarium—a method for direct observation of the brain: Ii. cranial trauma and brain movement. *Journal of Neurosurgery*, 3(6):487–505.

Shelden, C. H., Pudenz, R. H., Restarski, J. S., and Craig, W. M. (1944). The lucite calvarium—a method for direct observation of the brain: I. the surgical and lucite processing techniques. *Journal of Neurosurgery*, 1(1):67–75.

Takhounts, E. G., Ridella, S. A., Hasija, V., Tannous, R. E., Campbell, J. Q., Malone, D., Danelson, K., Stitzel, J., Rowson, S., and S., D. (2008). Investigation of traumatic brain injuries using the next generation of simulated injury monitor (simon) finite element head model. *Stapp Car Crash Journal*, 52:1–31.

Whyte, T., Liu, J., Chung, V., McErlane, S. A., Abebe, Z. A., McInnes, K. A., Wellington, C. L., and Cripton, P. A. (2019). Technique and preliminary findings for in vivo quantification of brain motion during injurious head impacts. *Journal of Biomechanics*, 95:109279.

Zhao, W., Cai, Y., Li, Z., and Ji, S. (2017). Injury prediction and vulnerability assessment using strain and susceptibility measures of the deep white matter. *Biomechanics and Modeling in Mechanobiology*, 16(5):1709–1727.

Zhao, W. and Ji, S. (2020). Displacement- and strain-based discrimination of head injury models across a wide range of blunt conditions. *Annals of Biomedical Engineering*, 8(9):1661–1677.

Zhou, Z., Li, X., Kleiven, S., Shah, C. S., and Hardy, W. N. (2019). A reanalysis of experimental brain strain data: Implication for finite element head model validation. *In SAE 62nd Stapp Car Crash Conference*.